RESEARCH ARTICLE

An Energy Model-Based Controller for a Three-Phase Grid-Tied Modular Multilevel Converter

GLENDY ANYALI CATZIN-CONTRERAS[1], (Member, IEEE),
GERARDO ESCOBAR[1], (Senior Member, IEEE),
JESUS ELIAS VALDEZ-RESENDIZ[1], (Senior Member, IEEE),
LUIS IBARRA[2], (Senior Member, IEEE),
AND ANDRES A. VALDEZ-FERNANDEZ[3], (Senior Member, IEEE)

[1]School of Engineering and Sciences, Tecnologico de Monterrey, Monterrey 64849, Mexico
[2]Tecnologico de Monterrey, Institute of Advanced Materials for Sustainable Manufacturing, Mexico City 14380, Mexico
[3]School of Sciences, Universidad Autonoma de San Luis Potosi, San Luis Potosi 78295, Mexico

Corresponding author: Gerardo Escobar (gerardo.escobar@tec.mx)

ABSTRACT This paper presents the modeling, control and evaluation in a real-time simulation (RTS) of a three-phase multilevel inverter based on the modular multilevel converter (MMC) topology. The developed model for MMC includes four decoupled state variables per phase, which are instrumental for the control design, namely injected (output) current, circulating current, total energy, and energy balance between arms. Based on this model, a control scheme is proposed with the aim to regulate and balance the total energy on each converter's phase, regulate the circulating currents, and inject a three-phase current synchronized with the grid voltage. As part of the control process, the proposed controller generates the reference for a modulation scheme to obtain the switching sequence for each converter's cell, which, in this case, is the phase-shifted carrier-based pulse-width modulation (PSC-PWM). As it was already reported in the literature, this particular modulation guarantees self (natural) balance of all capacitor voltages, i.e., they converge to the same steady-state average value without the need of any external balancing controller.

INDEX TERMS Modular multilevel converter, phase-shifted carrier-based pulse-width modulation, real-time simulation.

NOMENCLATURE

C	Cell capacitance.
$\mathbf{e}_{D\alpha\beta}$	Vector of differences between inserted voltages of lower and upper arms, $\mathbf{e}_{D\alpha\beta} \triangleq [e_{D\alpha}, e_{D\beta}]^\top$.
$\mathbf{e}_{D123}$	Vector of differences between inserted voltages of lower and upper arms $\mathbf{e}_{D123} \triangleq [e_{D1}, e_{D2}, e_{D3}]^\top$.
$\mathbf{e}_{N123}$	Vector of total inserted voltages of lower arms, $\mathbf{e}_{N123} \triangleq [e_{N1}, e_{N2}, e_{N3}]^\top$.
$\mathbf{e}_{P123}$	Vector of total inserted voltages of upper arms, $\mathbf{e}_{P123} \triangleq [e_{P1}, e_{P2}, e_{P3}]^\top$.
$\mathbf{e}_{T123}$	Vector of total inserted voltages per phase, $\mathbf{e}_{T123} \triangleq [e_{T1}, e_{T2}, e_{T3}]^\top$.
f_c	PSC-PWM carrier frequency.
f_s	Controller sampling frequency.

f_0	Grid fundamental frequency.
i	ith cell in a given phase, $i \in \{1, \ldots, 2n\}$.
$\mathbf{i}_{0123}$	Vector of injected currents, $\mathbf{i}_{0123} \triangleq [i_{01}, i_{02}, i_{03}]^\top$.
$\mathbf{i}_{0123}^*$	Vector of injected currents references, $\mathbf{i}_{0123}^* \triangleq [i_{01}^*, i_{02}^*, i_{03}^*]^\top$.
$\mathbf{i}_{0\alpha\beta}$	Vector of injected currents, $\mathbf{i}_{0\alpha\beta} \triangleq [i_{0\alpha}, i_{0\beta}]^\top$.
$\mathbf{i}_{0\alpha\beta}^*$	Vector of injected currents references, $\mathbf{i}_{0\alpha\beta}^* \triangleq [i_{0\alpha}^*, i_{0\beta}^*]^\top$.
$\tilde{\mathbf{i}}_{0\alpha\beta}$	Vector of injected currents tracking error, $\tilde{\mathbf{i}}_{0\alpha\beta} \triangleq [\tilde{i}_{0\alpha}, \tilde{i}_{0\beta}]^\top$.
$\mathbf{i}_{N123}$	Vector of lower arm currents, $\mathbf{i}_{N123} \triangleq [i_{N1}, i_{N2}, i_{N3}]^\top$.

The associate editor coordinating the review of this manuscript and approving it for publication was N. Prabaharan.

$\mathbf{i}_{P123}$ Vector of upper arm currents, $\mathbf{i}_{P123} \triangleq [i_{P1}, i_{P2}, i_{P3}]^\top$.

$\mathbf{i}_{T123}$ Vector of circulating currents, $\mathbf{i}_{T123} \triangleq [i_{T1}, i_{T2}, i_{T3}]^\top$.

$\mathbf{i}^*_{T123}$ Circulating currents loop - references vector, $\mathbf{i}^*_{T123} \triangleq [i^*_{T1}, i^*_{T2}, i^*_{T3}]^\top$.

$\tilde{\mathbf{i}}_{T123}$ Circulating currents loop - tracking errors vector, $\tilde{\mathbf{i}}_{T123} \triangleq [\tilde{i}_{T1}, \tilde{i}_{T2}, \tilde{i}_{T3}]^\top$.

j jth phase, $j \in \{1, 2, 3\}$.

k_{iD} Energy balance loop - integral gain.

k_{pD} Energy balance loop - proportional gain.

k_{iT} Energy regulation loop - integral gain.

k_{pT} Energy regulation loop - proportional gain.

L Arm inductance.

n Number of cells per arm.

P_{Dj} Energy balance loop - jth outcome.

P_0 Injected current loop - constant load power reference.

R_D Injected current loop - damping gain.

R_T Circulating current loop - damping gain.

u_{ij} ith switching signal in the jth phase.

v_{Cij} i capacitor voltage in the jth phase.

$v_{S,RMS}$ Grid voltage line-to-line RMS voltage

$\mathbf{v}_{S\alpha\beta}$ Vector of grid voltages, $\mathbf{v}_{S\alpha\beta} \triangleq [v_{S\alpha}, v_{S\beta}]^\top$.

$\mathbf{v}_{S123}$ Vector of grid voltages, $\mathbf{v}_{S123} = [v_{S1}, v_{S2}, v_{S3}]^\top$.

z_{Dj} Difference between upper and lower arms scaled energy of the jth phase.

z_{ij} ith capacitor scaled energy in the jth phase.

z_{Nj} Lower arm scaled energy in the jth phase.

z_{Pj} Upper arm scaled energy in the jth phase.

z_{Tj} Total scaled energy in the jth phase.

$\tilde{z}_{Dj}$ Energy balance loop - tracking error.

$\langle z_{Dj} \rangle_{1st}$ Energy balance loop - fundamental component of z_{Dj}.

z^*_{Tj} Energy regulation loop - reference for z_{Tj}.

$\tilde{z}_{Tj}$ Energy regulation loop - error.

$\langle z_{Tj} \rangle_{2nd}$ Energy regulation loop - second harmonic component of z_{Tj}.

γ_D Energy balance loop - notch filter gain.

γ_T Energy regulation loop - notch filter gain.

δ_{ij} ith cell duty ratio of the jth phase.

σ_D Injected current loop - resonant filter estimation gain.

σ_T Circulating current loop - resonant filter estimation gain.

Υ_{T123} Energy regulation loop - outcome vector, $\Upsilon_{T123} = [\Upsilon_{T1}, \Upsilon_{T2}, \Upsilon_{T3}]^\top$.

ω_0 Grid fundamental frequency.

I. INTRODUCTION

Due to their modular and scalable structure, feasible technology and tolerance to faults [1], modular multilevel converters (MMC) have received a significant attention from the scientific community in emerging applications such as large-scale grid-connected photovoltaic (PV) systems [2],

[3]; ultra-high voltage direct current (UHVDC) transmission systems [4]; as well as traditional applications such as static synchronous compensator (STATCOM) [5]; adjustable speed drives [6], among others.

In particular, transformerless half-bridge MMC topologies have become popular in medium and high-power applications [5], [7], where the number of cells increases and, consequently, the modulation scheme, modeling process, and control design become more convoluted [8], [9], [10]. Hence, much of the research works on MMC topologies have addressed topics such as modulation issues [11], modeling techniques [12], and control oriented issues such as tracking of the output current and regulation of the so-called circulating currents [3], besides the voltage (or energy) regulation and balance of capacitors voltages of every cell [8], [9], [10], [13], [14], [15], [16], [17], [18], [19], [20], [21].

In [8], the authors proposed a controller comprising proportional-plus-resonant (PR) and feedforward terms to solve the output current tracking, while the circulating current was regulated using a proportional action plus a feedforward term; [13] and [14] proposed a proportional plus integral (PI) controller for the regulation of circulating currents; [10] applied a linear extended state observer and a linear state error feedback to control circulating and output currents; [15] designed a proportional controller and a PI controller for the control of the arm differential energy and the arm-accumulated energy, respectively; [21] proposed a sorting algorithm and a level shifted modulation to guarantee capacitor voltage balance. In [9] and [16], feedforward and PR terms were applied to control output and circulating currents, while PI controllers were used in the energy regulation and balance loops; [17] proposed a direct multivariable control for output and circulating currents in combination with a sorting algorithm for capacitor voltages; and [18], [19], [20], [22] relied on model predictive control (MPC) combined with other technique to tackle all control issues on MMC; [18] used MPC for output and circulating currents, and the capacitor voltage balancing was left to the so-called nearest-level control; MPC in [19] was employed to control the arm currents, while a balancing control and the phase-shifted carrier-based pulse-width modulation (PSC-PWM) was applied to capacitor voltages; [20] also used MPC for circulating currents, and a voltage balancing algorithm for the capacitors, while a modulated MPC with bound-constrained quadratic programming (QP) is proposed in [22] to try to obtain an optimal solution.

The present paper focuses on the modeling, control, and evaluation of a three-phase MMC in a grid-tied inverter configuration for grid power injection. This work represents an extension of the single-phase solution reported in [9], now to the three-phase case. Instrumental for the control design is the development of a particular model for the MMC expressed in terms of four decoupled state variables per phase, referred to as injected (or output) current to the grid, circulating current, total energy, and energy balance

between arms, which are also considered as the controlled variables. Based on this model, a control scheme comprising four loops, one per those decoupled state variables, is proposed, which guarantees grid power injection through a three-phase current (synchronized with the grid voltage), tracking of the circulating currents toward appropriately defined references, as well as regulation of the total energy on each converter's phase, and balance of the energy among arms.

The regulation and balance of every capacitor voltage was left to the modulation scheme, which is in charge of generating the switching sequence for each converter's cell. In this case, a PSC-PWM scheme is considered as it provides a natural balancing mechanism for the capacitor voltages [23], meaning that they converge to the same average value in steady-state without adding a dedicated controller for them.

Summarizing, the following main contributions have been identified in the present work:

(1) A systematic framework for the mathematical modelling of a three-phase MMC topology, where the model is expressed in quite convenient variables for the control design.

(2) An overall control design process guaranteeing tracking of the output and circulating currents towards appropriately designed references, as well as energy (voltage) regulation and energy (voltage) balance of the MMC arms. Moreover, the proposed controller is combined with the PSC-PWM scheme to achieve individual capacitor voltage regulation at a cell level.

(3) Explicit tuning rules for every control parameter involved.

(4) Analysis of the harmonic contents of the energy variables showing that the difference between the energies of the upper and lower arms of each phase contains a fundamental component, while the sum of the energies in both upper and lower arms of each phase contains a second harmonic of the fundamental source frequency.

The evaluation of the closed loop, comprising the plant, the proposed control, and the PSC-PWM schemes, was performed trough a real-time simulation (RTS) based on the DS1007 board from dSPACE. This evaluation considers an MMC with three cells on each arm (n=3), 18 cells total. The performed tests include responses to load step changes as well as responses to unbalanced conditions in the capacitor voltages.

The rest of the paper is organized as follows. Section II presents the decoupled mathematical model for the three-phase MMC, and establishes the control objectives. Section III shows the control design for the MMC, the tuning rules for the involved control parameters, and the harmonic content in the energy variables. Section IV presents the RTS results of the MMC operating with the control and PSC-PWM schemes. Finally, Section V provides some concluding remarks.
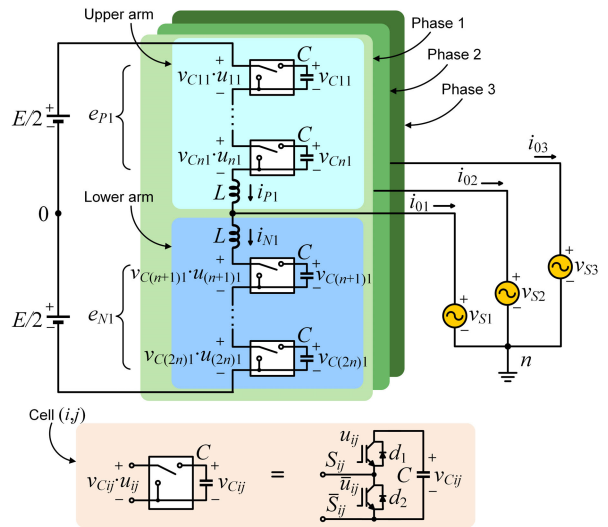

FIGURE 1. Topology of the three-phase MMC of 2n+1 levels.

II. SYSTEM MODEL

Figure 1 shows a three-phase three-wire grid-connected MMC comprising two arms per phase, namely, the upper and lower arms. Each arm contains a series connection of n half-bridges, referred to as cells or submodules, and terminated with an inductor. In total, there are $2n$ cells per branch, and 3 branches, which makes a total of $6n$ cells. Each cell comprises a capacitor that can be connected or bypassed using a one-pole-two-way switch made out of two complementary IGBTs (with corresponding free-wheeling diodes); in other words, the capacitor voltage can be either inserted or bypassed contributing or not with a voltage to the corresponding arm.

Figure 2 shows the four possible modes for cell (i, j) of the MMC, which depend on the two switching positions and the current's direction. If the upper switch S_{ij} is ON, then the capacitor voltage is inserted to the arm. This holds true independently of the current direction, i.e., the current can flow out of the terminal marked as positive through the IGBT (Figure 2a) or through the diode d_1 if its direction is reversed (Figure 2b). However, if the lower switch $\bar{S}_{ij}$ is ON, then the capacitor is bypassed irrespective of the current direction (Figures 2c and 2d); consequently, the voltage at the cell terminals is zero.

From now on, index $i \in \{1, \ldots, 2n\}$ is used to indicate the ith cell in a given phase. Moreover, cells may be grouped in upper and lower arm, and thus $i \in \{1, \ldots, n\}$ will be used for the upper arm, while $i \in \{n+1, \ldots, 2n\}$ for the lower arm. This will be explicitly indicated whenever needed. Hereinafter, index $j \in \{1, 2, 3\}$ is used to indicate the jth phase; therefore, there will not be explicit indication of this in the rest of the expressions unless necessary.

1) MAIN ASSUMPTIONS

Throughout the paper, the following considerations and assumptions are used to facilitate the modeling process, transformations and control design:
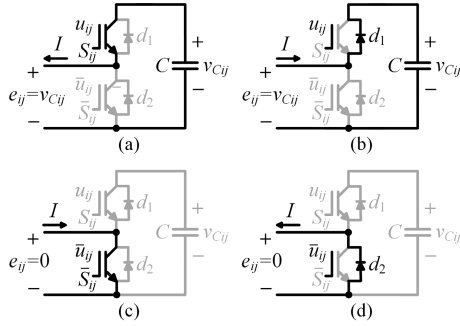
FIGURE 2. Different current paths in cell (i, j) of the MMC showing whether the capacitor is inserted ((a) and (b)) or bypassed ((c) and (d)).

A1 Since a three-wire grid connection is considered, then the sum of the injected currents is zero, i.e., $i_{01} + i_{02} + i_{03} = 0$.

A2 The three-phase voltage source $\mathbf{v}_{S123}$ is balanced, in the sense that $v_{S1} + v_{S2} + v_{S3} = 0$, i.e., the voltage source does not include a homopolar component.

A3 All inductors have the same inductance value L.

A4 The RMS voltage $v_{S,RMS}$ and the system's frequency ω_0 are known constants.

A5 The system parameters C, L, E are unknown constants.

The mathematical model of the MMC system in Figure 1 is described by expressions (1)-(3), which can be obtained by direct application of Kirchhoff's laws.

$$L\dot{\hat{\mathbf{i}}}_{P123} = \tfrac{1}{2}\mathbf{E} - \mathbf{v}_{n0} - \mathbf{v}_{S123} - \mathbf{e}_{P123}, \qquad (1)$$

$$L\dot{\hat{\mathbf{i}}}_{N123} = \tfrac{1}{2}\mathbf{E} + \mathbf{v}_{n0} + \mathbf{v}_{S123} - \mathbf{e}_{N123}, \qquad (2)$$

$$C\dot{v}_{Cij} = \begin{cases} i_{Pj} \cdot u_{ij}, & i \in \{1, \ldots, n\}, \\ i_{Nj} \cdot u_{ij}, & i \in \{n+1, \ldots, 2n\}, \end{cases} \qquad (3)$$

where L and C are the inductance and capacitance values, respectively; $\mathbf{i}_{P123} \triangleq [i_{P1}, i_{P2}, i_{P3}]^{\top}$ and $\mathbf{i}_{N123} \triangleq [i_{N1}, i_{N2}, i_{N3}]^{\top}$ represent the vectors of the upper and lower arm currents, respectively; $\mathbf{E} = [E, E, E]^{\top}$ represents the vector of the DC-link voltage; $\mathbf{v}_{n0} = [v_{n0}, v_{n0}, v_{n0}]^{\top}$ is the vector of the voltage drop between point n and point 0 (see Figure 1); $\mathbf{v}_{S123} = [v_{S1}, v_{S2}, v_{S3}]^{\top}$ is the vector of the grid voltage; $\mathbf{e}_{P123} \triangleq [e_{P1}, e_{P2}, e_{P3}]^{\top}$ and $\mathbf{e}_{N123} \triangleq [e_{N1}, e_{N2}, e_{N3}]^{\top}$ are the vectors of the total inserted voltages at the upper and lower arms, which are given by

$$e_{Pj} \triangleq \sum_{i=1}^{n} v_{Cij} \cdot u_{ij}, \quad e_{Nj} \triangleq \sum_{i=n+1}^{2n} v_{Cij} \cdot u_{ij}, \qquad (4)$$

where v_{Cij} and $u_{ij}(u_{ij} \in \{0, 1\})$ are the ith capacitor voltage $(i \in \{1, \ldots, 2n\})$ and corresponding switching signal of the jth phase, respectively.

A. INJECTED CURRENTS' DYNAMICS

The vector of injected currents (to the grid) $\mathbf{i}_{0123} \triangleq [i_{01}, i_{02}, i_{03}]^{\top}$ is defined as the difference between the upper and lower arm currents vectors, i.e., $\mathbf{i}_{0123} \triangleq \mathbf{i}_{P123} - \mathbf{i}_{N123}$, which

can also be interpreted as a differential-mode currents vector, and whose dynamics, based on (1) and (2), is described by

$$L\dot{\hat{\mathbf{i}}}_{0123} = \mathbf{e}_{D123} - 2\mathbf{v}_{n0} - 2\mathbf{v}_{S123}, \qquad (5)$$

where $\mathbf{e}_{D123} \triangleq [e_{D1}, e_{D2}, e_{D3}]^{\top}$ represents the difference between the vectors of voltages produced by the lower and upper arms, and thus it can be interpreted as a differential-mode inverter voltages vector, i.e.,

$$\mathbf{e}_{D123} \triangleq \mathbf{e}_{N123} - \mathbf{e}_{P123}; \qquad (6)$$

and $\mathbf{v}_{n0} = [v_{n0}, v_{n0}, v_{n0}]^{\top}$, with v_{n0} given by

$$v_{n0} = \tfrac{1}{6}(e_{D1} + e_{D2} + e_{D3}). \qquad (7)$$

Direct substitution of (7) in (5) yields

$$L\dot{\hat{\mathbf{i}}}_{0123} = \mathbf{B}\mathbf{e}_{D123} - 2\mathbf{v}_{S123}, \qquad (8)$$

with

$$\mathbf{B} \triangleq \frac{1}{3}\begin{bmatrix} 2 & -1 & -1 \\ -1 & 2 & -1 \\ -1 & -1 & 2 \end{bmatrix}.$$

Based on assumptions **A1** and **A2**, the model (8) can be expressed in terms of (fixed-reference frame) $\alpha\beta$-coordinates as follows:

$$L\dot{\hat{\mathbf{i}}}_{0\alpha\beta} = \mathbf{e}_{D\alpha\beta} - 2\mathbf{v}_{S\alpha\beta}, \qquad (9)$$

where the following Clarke's transformation has been considered:

$$\mathbf{x}_{\alpha\beta} = \mathbf{T}\mathbf{x}_{123}, \qquad (10)$$

where $\mathbf{x}_{\alpha\beta} = [x_{\alpha}, x_{\beta}]^{\top}$, $\mathbf{x}_{123} = [x_1, x_2, x_3]^{\top}$ ($\mathbf{x}$ can represent either $\mathbf{i}_0$, $\mathbf{v}_S$ or $\mathbf{e}_D$), and

$$\mathbf{T} = \sqrt{\frac{2}{3}}\begin{bmatrix} 1 & -1/2 & -1/2 \\ 0 & \sqrt{3}/2 & -\sqrt{3}/2 \end{bmatrix}, \qquad (11)$$

which corresponds to a three-to-two power-invariant Clarke's transformation, where the homopolar component has been disregarded based on assumption **A1**. Moreover, the properties $\mathbf{T}^{-1} = \mathbf{T}^{\top}$ and $\mathbf{T}\mathbf{B}\mathbf{T}^{-1} = \mathbf{I}_2$, with $\mathbf{I}_2$ representing the 2×2 identity matrix, have been used to obtain (9).

B. CIRCULATING CURRENTS' DYNAMICS

The vector of circulating currents $\mathbf{i}_{T123} \triangleq [i_{T1}, i_{T2}, i_{T3}]^{\top}$ is defined as the sum of the upper and lower arm currents, i.e., $\mathbf{i}_{T123} \triangleq \mathbf{i}_{P123} + \mathbf{i}_{N123}$, which can also be interpreted as common-mode currents vector, and whose dynamics, based on (1) and (2) is described by

$$L\dot{\hat{\mathbf{i}}}_{T123} = \mathbf{E} - \mathbf{e}_{T123}, \qquad (12)$$

where $\mathbf{e}_{T123} \triangleq [e_{T1}, e_{T2}, e_{T3}]^{\top}$ represents the vector of total inserted voltages produced by the upper and lower cells, which can be interpreted as a common-mode inverter voltages vector, i.e.,

$$\mathbf{e}_{T123} \triangleq \mathbf{e}_{P123} + \mathbf{e}_{N123}. \qquad (13)$$

C. CAPACITORS' VOLTAGE DYNAMICS

Considering the following variable transformation

$$z_{ij} \triangleq \tfrac{1}{2} v_{Cij}^2, \quad i \in \{1, \dots, 2n\}, \tag{14}$$

then the capacitor voltage dynamics (3) can be rewritten as

$$C\dot{z}_{ij} = \begin{cases} i_{Pj} \cdot v_{Cij} \cdot u_{ij}, & i \in \{1, \dots, n\}, \\ i_{Nj} \cdot v_{Cij} \cdot u_{ij}, & i \in \{n+1, \dots, 2n\}. \end{cases} \tag{15}$$

Notice that Cz_{ij} represents the energy of the ith capacitor ($i \in \{1, \dots, 2n\}$) in the jth phase, while z_{ij} is just a scaled version, which explains why this new system description is referred to as the *capacitors' energy dynamics* in previous works [24], [25].

So far, system (15) is of order $6n$. In what follows, a change of variables is proposed to reduce the order of the system, and thus the control design problem. These new variables are defined as the accumulated energies of the upper and lower arms, i.e.,

$$z_{Pj} \triangleq \sum_{i=1}^{n} z_{ij}, \quad z_{Nj} \triangleq \sum_{i=n+1}^{2n} z_{ij}. \tag{16}$$

Out of this, the model (15) is reduced to

$$C\dot{z}_{Pj} = i_{Pj} \cdot e_{Pj}, \quad C\dot{z}_{Nj} = i_{Nj} \cdot e_{Nj}. \tag{17}$$

Notice that the order of the system has been reduced from $6 \times n$ in (15) to simply 6 in (17), i.e., the total number of arms. In what follows, the control design focuses on the control of the energy per arm, or equivalently, on the total inserted voltage per arm rather than on the individual capacitor voltages. The regulation and balance of the individual capacitors voltages is left to the natural balancing capability of the modulation scheme PSC-PMW under certain conditions [23].

Furthermore, to facilitate the controller design, it is convenient to express (17) in terms of new variables defined as

$$z_{Tj} \triangleq z_{Pj} + z_{Nj}, \tag{18}$$

$$z_{Dj} \triangleq z_{Pj} - z_{Nj}, \tag{19}$$

where Cz_{Tj} represents the total accumulated energy of capacitors in both upper and lower arms of the jth phase, while Cz_{Dj} represents the difference between the energies of the upper and lower arms of the jth phase. Out of these definitions, (17) can be rewritten as

$$C\dot{z}_{Tj} = i_{Pj} \cdot e_{Pj} + i_{Nj} \cdot e_{Nj}, \tag{20}$$

$$C\dot{z}_{Dj} = i_{Pj} \cdot e_{Pj} - i_{Nj} \cdot e_{Nj}, \tag{21}$$

which, in terms of i_{Tj}, i_{0j}, e_{Tj} and e_{Dj}, can also be written as

$$C\dot{z}_{Tj} = \tfrac{1}{2} \left[i_{Tj} \cdot e_{Tj} - i_{0j} \cdot e_{Dj} \right], \tag{22}$$

$$C\dot{z}_{Dj} = \tfrac{1}{2} \left[i_{0j} \cdot e_{Tj} - i_{Tj} \cdot e_{Dj} \right]. \tag{23}$$

D. CONTROL OBJECTIVES

Based on the transformed model comprising (9), (12), (22), and (23), the control objectives can be established as follows:

1) *Injected current loop.* The grid current $\mathbf{i}_{0\alpha\beta}$ must asymptotically track a reference $\mathbf{i}_{0\alpha\beta}^*$, i.e.,

$$\mathbf{i}_{0\alpha\beta} \rightarrow \mathbf{i}_{0\alpha\beta}^* = \frac{P_0}{v_{S,RMS}^2} \mathbf{v}_{S\alpha\beta} \quad \text{as} \quad t \rightarrow \infty, \tag{24}$$

where $\mathbf{v}_{S\alpha\beta}$ is the grid voltage in $\alpha\beta$-coordinates, P_0 is the constant power reference, and $v_{S,RMS}$ is the line-to-line RMS voltage of $\mathbf{v}_{S123}$. This control objective can also be expressed in terms of the original three-phase coordinates, i.e.,

$$\mathbf{i}_{0123} \rightarrow \mathbf{i}_{0123}^* = \frac{P_0}{v_{S,RMS}^2} \mathbf{v}_{S123} \quad \text{as} \quad t \rightarrow \infty. \tag{25}$$

2) *Circulating current loop.* The circulating currents vector $\mathbf{i}_{T123}$ must asymptotically track a reference $\mathbf{i}_{T123}^*$, i.e.,

$$\begin{aligned} \mathbf{i}_{T123} &\rightarrow \mathbf{i}_{T123}^* \\ &= \Upsilon_{T123} \\ &\quad + \frac{\text{diag}\left([P_{D1}, P_{D2}, P_{D3}]\right)}{v_{S,RMS}^2} \mathbf{v}_{S123} \quad \text{as} \quad t \rightarrow \infty \end{aligned} \tag{26}$$

where, as as it will be described in the next section, $\Upsilon_{T123} = [\Upsilon_{T1}, \Upsilon_{T2}, \Upsilon_{T3}]^\top$ is the outcome of the voltage regulation loop, and vector $[P_{D1}, P_{D2}, P_{D3}]$ is the outcome of the voltage balance loop.

3) *Energy regulation loop.* The total accumulated energy must be regulated (in average) toward a constant reference per phase, i.e.,

$$z_{Tj} \rightarrow z_{Tj}^* = \frac{E^2}{n} \quad \text{as} \quad t \rightarrow \infty. \tag{27}$$

4) *Energy balance loop.* The energy difference of each phase must be zeroed (in average), i.e.,

$$z_{Dj} \rightarrow 0 \quad \text{as} \quad t \rightarrow \infty. \tag{28}$$

III. CONTROLLER DESIGN

It is here proposed to separate current and voltage stages such that, in close-loop, the inductor current dynamics evolve faster than the capacitor voltage dynamics. Therefore, using scale separation arguments, the controller design can be split in the current and voltage stages. The current stage comprises injected and circulating current loops, whereas the voltage stage comprises energy regulation and balance loops.

A. INJECTED CURRENT LOOP

The injected current loop design considers the subsystem (9). This controller aims to establish $\mathbf{e}_{D\alpha\beta}$ to force the grid current vector $\mathbf{i}_{0\alpha\beta}$ to follow $\mathbf{i}_{0\alpha\beta}^*$, described in (24). For this, subsystem (9) is expressed in terms of the increments $\tilde{\mathbf{i}}_{0\alpha\beta} \triangleq \mathbf{i}_{0\alpha\beta} - \mathbf{i}_{0\alpha\beta}^*$, i.e.,

$$L\dot{\tilde{\mathbf{i}}}_{0\alpha\beta} = \mathbf{e}_{D\alpha\beta} - 2\mathbf{v}_{S\alpha\beta} + \boldsymbol{\phi}_{D\alpha\beta} \tag{29}$$

where $\boldsymbol{\phi}_{D\alpha\beta} \triangleq -L\dot{\hat{\mathbf{i}}}^*_{0\alpha\beta}$. Based on the structure of the error model (29), the following controller is proposed

$$\mathbf{e}_{D\alpha\beta} = 2\mathbf{v}_{S\alpha\beta} - R_D\tilde{\mathbf{i}}_{0\alpha\beta} - \hat{\boldsymbol{\phi}}_{D\alpha\beta}, \tag{30}$$

which comprises a feedforward term $2\mathbf{v}_{S\alpha\beta}$; a damping term $R_D\tilde{\mathbf{i}}_{0\alpha\beta}$, where $R_D > 0$ is a damping gain; and a compensation term with a resonant structure:

$$\hat{\boldsymbol{\phi}}_{D\alpha\beta} = \text{diag}\left(\left[\frac{\sigma_D s}{s^2 + \omega_0^2}, \frac{\sigma_D s}{s^2 + \omega_0^2}\right]\right)\tilde{\mathbf{i}}_{0\alpha\beta}, \tag{31}$$

where $\sigma_D > 0$ is an estimation gain, $\omega_0 = 2\pi f_0$ is the grid voltage fundamental frequency in rad/s (f_0 is the fundamental frequency in Hz) and s is the complex variable. The compensation term $\hat{\boldsymbol{\phi}}_{D\alpha\beta}$ is aimed to estimate $\boldsymbol{\phi}_{D\alpha\beta}$ in (29), and thus, to cancel it out.

B. CIRCULATING CURRENT LOOP

The circulating current loop design considers (12). It aims to generate $\mathbf{e}_{T123}$ such that the circulating current vector $\mathbf{i}_{T123}$ follows its reference $\mathbf{i}^*_{T123}$, described in (26). To this end, subsystem (12) is expressed in terms of the increments $\tilde{\mathbf{i}}_{T123} \triangleq \mathbf{i}_{T123} - \mathbf{i}^*_{T123}$, yielding

$$L\dot{\tilde{\mathbf{i}}}_{T123} = \mathbf{E} - \mathbf{e}_{T123} + \boldsymbol{\phi}_{T123}, \tag{32}$$

with $\boldsymbol{\phi}_{T123} \triangleq -L\dot{\hat{\mathbf{i}}}^*_{T123}$. Based on the error model structure (32), the following controller is proposed:

$$\mathbf{e}_{T123} = \mathbf{E} + R_T\tilde{\mathbf{i}}_{T123} + \hat{\boldsymbol{\phi}}_{T123}, \tag{33}$$

which comprises a feedforward term $\mathbf{E}$; a damping term $R_T\tilde{\mathbf{i}}_{T123}$, where $R_T > 0$ is a damping gain; and a compensation term with the following resonant structure:

$$\hat{\boldsymbol{\phi}}_{T123} = \text{diag}\left(\left[\frac{\sigma_T s}{s^2 + \omega_0^2}, \frac{\sigma_T s}{s^2 + \omega_0^2}, \frac{\sigma_T s}{s^2 + \omega_0^2}\right]\right)\tilde{\mathbf{i}}_{T123}, \tag{34}$$

where σ_T is an estimation gain. The compensation term $\hat{\boldsymbol{\phi}}_{T123}$ is aimed to estimate $\boldsymbol{\phi}_{T123}$ in (32), and thus to cancel it out.

C. ENERGY REGULATION LOOP

The energy regulation loop considers the subsystem (22). It is assumed that the current control objectives are attained relatively quickly; therefore, based on scale separation, it is considered that after a relatively short time the following is achieved:

$$\mathbf{i}_{0123} \approx \mathbf{i}^*_{0123}, \quad \mathbf{i}_{T123} \approx \mathbf{i}^*_{T123}, \tag{35}$$

$$\hat{\boldsymbol{\phi}}_{D123} \approx \boldsymbol{\phi}_{D123}, \quad \hat{\boldsymbol{\phi}}_{T123} \approx \boldsymbol{\phi}_{T123}. \tag{36}$$

Out of these, the controller expressions (30) and (33) can be simplified as

$$\mathbf{e}_{D123} = 2\mathbf{v}_{S123} + L\dot{\hat{\mathbf{i}}}^*_{0123}, \tag{37}$$

$$\mathbf{e}_{T123} = \mathbf{E} - L\dot{\hat{\mathbf{i}}}^*_{T123}. \tag{38}$$

Using assumptions (35)-(36) and simplifications (37)-(38) in (22), and extracting the DC components of all terms on the right-hand-side (RHS) (recall that the control objective focuses on the regulation of z_{Tj} in average), yields

$$C\dot{z}_{Tj} = \frac{1}{2}\left\langle\left(\Upsilon_{Tj} + \frac{P_{Dj} \cdot v_{Sj}}{v^2_{S,RMS}}\right)\left(E - L\dot{\hat{i}}^*_{Tj}\right)\right\rangle_{\text{DC}} - \frac{1}{2}\left\langle\left(\frac{P_0 \cdot v_{Sj}}{v^2_{S,RMS}}\right)\left(2v_{Sj} + L\dot{\hat{i}}^*_{0j}\right)\right\rangle_{\text{DC}}, \tag{39}$$

$$C\dot{z}_{Tj} = \frac{E}{2}\Upsilon_{Tj} - \frac{1}{2}\left\langle\frac{2P_0 \cdot v_{Sj} \cdot v_{Sj}}{v^2_{S,RMS}}\right\rangle_{\text{DC}}$$

$$C\dot{z}_{Tj} = \frac{E}{2}\Upsilon_{Tj} - \frac{P_0}{3}, \tag{40}$$

where $\langle\cdot\rangle_{\text{DC}}$ represents an operator to extract the DC component of the argument; in particular, $\left\langle v^2_{Sj}\right\rangle_{\text{DC}} = v^2_{S,RMS}/3$. Notice that, Υ_{Tj} represents the actual control input of the jth phase, while $P_0/3$ represents an unknown constant perturbation.

Now, expressing (40) in terms of the increments $\tilde{z}_{Tj} \triangleq z_{Tj} - z^*_{Tj}$ yields the following set of decoupled first order systems (one per phase) perturbed by an unknown constant:

$$C\dot{\tilde{z}}_{Tj} = \frac{E}{2}\Upsilon_{Tj} - \frac{P_0}{3}. \tag{41}$$

Therefore, the following proportional plus integral (PI) controller (written in the s-domain) for the jth phase is proposed:

$$\Upsilon_{Tj} = -\left(k_{pT} + \frac{k_{iT}}{s}\right)\tilde{z}_{Tj}, \tag{42}$$

where $k_{pT} > 0$ and $k_{iT} > 0$ are the proportional and integral gains, respectively.

D. ENERGY BALANCE LOOP

The energy balance loop design involves subsystem (23). As in the voltage regulation loop, assumptions (35)-(36) and simplifications (37)-(38) are applied in (23), based on the accomplishment of the current's control objectives. If, only the DC component is considered, i.e., all harmonic perturbations are neglected, then the following reduced system can be obtained for the jth phase:

$$C\dot{z}_{Dj} = \frac{1}{2}\left\langle\left(\frac{P_0 \cdot v_{Sj}}{v^2_{S,RMS}}\right)\left(E - L\dot{\hat{i}}^*_{Tj}\right)\right\rangle_{\text{DC}} - \frac{1}{2}\left\langle\left(\Upsilon_{Tj} + \frac{P_{Dj} \cdot v_{Sj}}{v^2_{S,RMS}}\right)\left(2v_{Sj} + L\dot{\hat{i}}^*_{0j}\right)\right\rangle_{\text{DC}}, \tag{43}$$

$$C\dot{z}_{Dj} = -\frac{1}{2}\left\langle\frac{2P_{Dj} \cdot v_{Sj} \cdot v_{Sj}}{v^2_{S,RMS}}\right\rangle_{\text{DC}}$$

$$C\dot{z}_{Dj} = -\frac{1}{3}P_{Dj}, \tag{44}$$

where $\left\langle v^2_{Sj}\right\rangle_{\text{DC}} = v^2_{S,RMS}/3$ was used. Notice that P_{Dj} represents the actual control input of the jth phase.

Now, expressing (44) in terms of the increments $\tilde{z}_{Dj} \triangleq z_{Dj} - z_{Dj}^* = z_{Dj}$ yields the following set of decoupled first order systems (one per phase):

$$C\dot{\tilde{z}}_{Dj} = -\frac{1}{3}P_{Dj}. \tag{45}$$

Therefore, the following PI controller is proposed for the jth phase:

$$P_{Dj} = \left(k_{pD} + \frac{k_{iD}}{s}\right)\tilde{z}_{Dj}, \tag{46}$$

where $k_{pD} > 0$ and $k_{iD} > 0$ are the proportional and integral gains, respectively.

Remark 1: As it will be shown in Section III-F, for the jth phase, signals z_{Tj} are mainly polluted by second order harmonics, while signals z_{Dj} are mainly polluted by fundamental components. Therefore, to avoid propagation of such disturbances through the controller, it is suggested to filter them out by means of the following notch filters tuned at those specific harmonics:

$$\langle z_{Tj}\rangle_{\text{2nd}} = \left(\frac{s^2 + 4\omega_0^2}{s^2 + \gamma_T s + 4\omega_0^2}\right)z_{Tj}, \tag{47}$$

$$\langle z_{Dj}\rangle_{\text{1st}} = \left(\frac{s^2 + \omega_0^2}{s^2 + \gamma_D s + \omega_0^2}\right)z_{Dj}, \tag{48}$$

where γ_T and γ_D are the gains that define the speed of response and selectivity of these filters. Cleaned signals $\langle z_{Tj}\rangle_{\text{2nd}}$ and $\langle z_{Dj}\rangle_{\text{1st}}$ can now be used in the place of z_{Tj} and z_{Dj} ($j \in \{1, 2, 3\}$) to compute the error signals involved in controllers (42) and (46).

Once $\mathbf{e}_{T123}$ and $\mathbf{e}_{D123}$ are obtained, the original vectors of the total inserted voltages in upper and lower arms $\mathbf{e}_{P123}$ and $\mathbf{e}_{N123}$, respectively, can be recuperated out of definitions (6) and (13) as follows:

$$\mathbf{e}_{P123} = \frac{\mathbf{e}_{T123} - \mathbf{e}_{D123}}{2}, \quad \mathbf{e}_{N123} = \frac{\mathbf{e}_{T123} + \mathbf{e}_{D123}}{2}. \tag{49}$$

As described in [9], and based on (4), the duty ratios can be calculated as

$$\delta_{ij} = \begin{cases} \frac{e_{Pj}}{n \cdot v_{Cij}}, & i \in \{1, \ldots, n\}, \\ \frac{e_{Nj}}{n \cdot v_{Cij}}, & i \in \{n+1, \ldots, 2n\}. \end{cases} \tag{50}$$

Finally, the original switching control signals u_{ij} ($i \in \{1, \ldots, 2n\}$, $j \in \{1, 2, 3\}$) can be recovered out of a PSC-PWM scheme using duty ratios (50). Recall that the PSC-PWM was chosen as it guarantees a natural balancing mechanism of the cells' voltages. Summarizing, the overall proposed controller is composed by the loops of injected and circulating currents (30)-(31) and (33)-(34), respectively; the loops of energy regulation and balance (42) and (46), respectively; the notch filters for cleaning the energy signals (47) and (48); the transformation of variables (16), (18)-(19); the references for each arm (49), and the references for each cell (50). A block diagram of the overall proposed controller is shown in Figure 3.

E. CONTROL PARAMETERS' TUNING

The current control loop parameters' tuning follows from similar ideas as in [8]; here, for the sake of brevity, only the results are presented. The interested reader can consult the details about the parameters' derivation in [8].

The proportional gain and the resonant filter's gain σ_D at the output current loop was set to

$$R_D \leq \frac{\pi f_s L}{5}, \quad \sigma_D = \frac{2.2}{T_r}, \tag{51}$$

where f_s is the sampling frequency of the controller implementation; T_r is the desired rise time for the (envelope of the) estimated harmonic component, evaluated between 10% and 90% of a step response of the amplitude of the corresponding sinusoidal perturbation.

In their turn, the gains in the circulating current loop, R_T and σ_T, were set using similar expressions to (51), i.e.,

$$R_T \leq \frac{\pi f_s L}{5}, \quad \sigma_T = \frac{2.2}{T_r}. \tag{52}$$

The tuning rules of parameters k_{pT} and k_{iT} of the energy regulation loop can be obtained from the characteristic polynomial of the closed loop between system (41) and controller (42):

$$s^2 + \frac{Ek_{pT}}{2C}s + \frac{Ek_{iT}}{2C} = 0, \tag{53}$$

where the natural frequency is given by $\omega_{nzT} = \sqrt{Ek_{iT}/(2C)}$ and the damping ratio is $\zeta_{zT} = Ek_{pT}/\sqrt{8CEk_{iT}}$. According to [26], if the damping ratio is restricted to $\zeta_{zT} \geq 1/\sqrt{2}$, then the bandwidth of the energy regulation dynamics is limited to $BW_{zT} \leq \omega_{nzT}$. It is proposed here to restrict the bandwidth as $BW_{zT} \leq \omega_0/6$. In this way, k_{pT} and k_{iT} can be set as

$$k_{pT} \geq \frac{2C\omega_0}{3\sqrt{2}E}, \quad k_{iT} \leq \frac{C\omega_0^2}{18E}. \tag{54}$$

The tuning of the energy balance loop parameters can be obtained using the following characteristic polynomial that results from the closed loop between system (45) and controller (46):

$$s^2 + \frac{k_{pD}}{3C}s + \frac{k_{iD}}{3C} = 0, \tag{55}$$

where the natural frequency is $\omega_{nzD} = \sqrt{k_{iD}/(3C)}$ and the damping ratio is $\zeta_{zD} = k_{pD}/\sqrt{12Ck_{iD}}$. As in the energy regulation loop, if the damping ratio is restricted to be $\zeta_{zD} \geq 1/\sqrt{2}$, then the bandwidth of the energy balance dynamics is limited to $BW_{zD} \leq \omega_{nzD}$. Moreover, the dynamics of this loop must be the slowest of the overall control scheme. In this case, a bandwidth of 2 Hz has been selected, i.e., $BW_{zD} \leq 4\pi$. Out of this, k_{pD} and k_{iD} can be fixed according to

$$k_{pD} \geq \frac{24\pi C}{\sqrt{2}}, \quad k_{iD} \leq 48\pi^2 C. \tag{56}$$
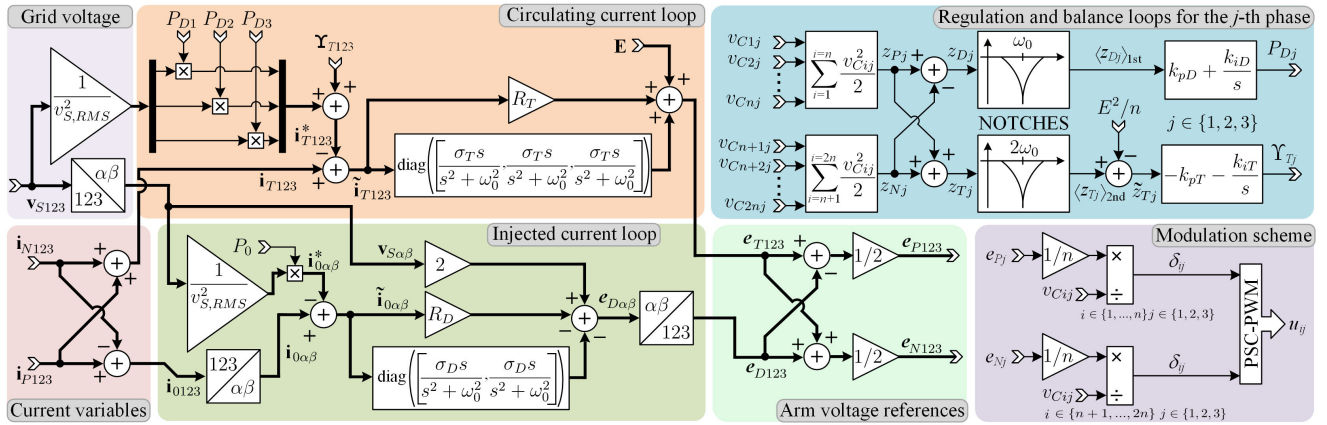
FIGURE 3. Block diagram of the overall proposed controller.

Finally, following the ideas in [27], the parameters in the notch filters (47) and (48) can be tuned according to

$$\gamma_T \le \frac{9}{T_{sT}}, \quad \gamma_D \le \frac{9}{T_{sD}} \tag{57}$$

where $T_{sT}=2.25/\omega_0$ and $T_{sD}=4.5/\omega_0$ represent the settling times of systems (47) and (48), respectively.

F. HARMONIC COMPONENTS IN THE ENERGY VARIABLES

Energy variables z_{Tj} and z_{Dj}, for the jth phase, in the steady state, are not purely DC signals, but they contain a second and a first harmonic, respectively, as it will be shown next. Dynamic models describing z_{Tj} (22) and z_{Dj} (23) are linear systems, then, superposition can be applied and general expressions for both signals (in the steady state) can be decomposed as

$$\bar{z}_{Tj} = \langle \bar{z}_{Tj} \rangle_{\text{DC}} + \langle \bar{z}_{Tj} \rangle_{\text{AC}}, \tag{58}$$

$$\bar{z}_{Dj} = \langle \bar{z}_{Dj} \rangle_{\text{DC}} + \langle \bar{z}_{Dj} \rangle_{\text{AC}}, \tag{59}$$

where $\langle \cdot \rangle_{\text{DC}}$ and $\langle \cdot \rangle_{\text{AC}}$ represent the DC and AC components of the argument. In what follows, DC component, average or equilibrium of a variable are used indistinctly, whenever dealing with the regulation issues. Hereinafter, a bar above a variable, i.e., $\overline{(\cdot)}$ stands for a steady-state expression. For the sake of brevity, the analysis below only considers phase one of the MMC as an example. The same steps can be followed for the other two phases, with the appropriate definitions for the involved variables and, in particular, for the grid voltage.

1) DC COMPONENTS IN Z_{T1} AND Z_{D1}

The DC component of $\bar{z}_{T1}$ is obtained from the closed loop between the error model (41) and the PI controller (42) expressed as $\Upsilon_{T1} = -k_{pT}\tilde{z}_{T1} - k_{iT}\xi$ and $\dot{\xi} = \tilde{z}_{T1}$. This yields the following state-space dynamical representation:

$$\begin{bmatrix} \dot{\tilde{z}}_{T1} \\ \dot{\xi} \end{bmatrix} = \begin{bmatrix} -\frac{Ek_{pT}}{2C} & -\frac{Ek_{iT}}{2C} \\ 1 & 0 \end{bmatrix} \begin{bmatrix} \tilde{z}_{T1} \\ \xi \end{bmatrix} + \begin{bmatrix} -\frac{P_0}{3C} \\ 0 \end{bmatrix}. \tag{60}$$

The equilibrium point of system (60) is given by $\begin{bmatrix} \bar{\tilde{z}}_{T1}, & \bar{\xi} \end{bmatrix} = [0, \ -2P_0/(3Ek_{iT})]$. The equilibrium point $\bar{\tilde{z}}_{T1} = 0$ implies that, at steady-state, the controlled variable z_{T1} has reached, in average, its reference value given in (27), that is, $\langle \bar{z}_{T1} \rangle_{\text{DC}} = E^2/n$.

Regarding the DC component of z_{D1}, the state-space representation of the closed loop between the error model (45) and the PI controller (46), expressed as $P_{D1} = k_{pD}\tilde{z}_{D1} + k_{iD}\chi$ and $\dot{\chi} = \tilde{z}_{D1}$, is given by

$$\begin{bmatrix} \dot{\tilde{z}}_{D1} \\ \dot{\chi} \end{bmatrix} = \begin{bmatrix} -k_{pD}/3C & -k_{iD}/3C \\ 1 & 0 \end{bmatrix} \begin{bmatrix} \tilde{z}_{D1} \\ \chi \end{bmatrix}. \tag{61}$$

The equilibrium point of system (61) is given by $\begin{bmatrix} \bar{\tilde{z}}_{D1}, & \bar{\chi} \end{bmatrix} = [0, \ 0]$. The equilibrium point $\bar{\tilde{z}}_{D1} = 0$ implies that, at steady-state, the controlled variable z_{D1} reaches, in average, its reference value stated in (28), that is, $\langle \bar{z}_{D1} \rangle_{\text{DC}} = 0$.

2) AC COMPONENTS IN Z_{T1} AND Z_{D1}

To determine the AC component of z_{T1} (see (58)), expression (22) is solved for the steady-state. For this, the steady state solutions of all involved variables on the RHS of (22) are calculated, and then used in this same expression. Finally, the resulting expression is integrated with respect to time disregarding initial conditions and DC components.

On the one hand, consider once more that, in the steady state, $\bar{\tilde{z}}_{T1} = 0$ and $\bar{\tilde{z}}_{D1} = 0$, and thus their time derivatives are also zero. Hence, after zeroing the error models (41) and (45), $\Upsilon_{T1}=2P_0/(3E)$ and $P_{D1}=0$. Consequently, the steady-state value for the circulating current $\bar{i}_{T1}$ equals the steady state value of its reference (26), which is given by $\bar{i}_{T1}^* = 2P_0/(3E)$, that is,

$$\bar{i}_{T1} = \bar{i}_{T1}^* = \frac{2P_0}{3E}, \tag{62}$$

and its controller (38) in steady-state $\bar{e}_{T1}$ reduces to

$$\bar{e}_{T1} = E. \tag{63}$$

On the other hand, consider that the output current in the steady state $\bar{i}_{01}$ has reached its reference i_{01}^* described in (25),

that is,

$$\bar{i}_{01} = i_{01}^* = \frac{P_0}{v_{S,RMS}^2} v_{S1}. \tag{64}$$

If the grid voltage is given by

$$v_{S1} = \sqrt{\frac{2}{3}} \, v_{S,RMS} \, \sin(\omega_0 t), \tag{65}$$

then its time derivative is given by

$$\dot{v}_{S1} = \omega_0 \varphi_1, \tag{66}$$

$$\varphi_1 \triangleq \sqrt{\frac{2}{3}} \, v_{S,RMS} \, \cos(\omega_0 t), \tag{67}$$

and thus the controller expression (see (37)) in steady state is given by

$$\bar{e}_{D1} = 2v_{S1} + \frac{LP_0\omega_0}{v_{S,RMS}^2}\varphi_1. \tag{68}$$

Direct substitution of (62)-(68) into (22) yields

$$2C\left\langle \dot{\bar{z}}_{T1} \right\rangle_{AC} = \frac{2P_0}{3} - \frac{2P_0 \cdot v_{S1}^2}{v_{S,RMS}^2} - \frac{LP_0^2\omega_0 \cdot \varphi_1 \cdot v_{S1}}{v_{S,RMS}^4}. \tag{69}$$

Notice that the above substitutions set the solution of (22) around $\langle \bar{z}_{T1} \rangle_{DC}$; therefore, (69) effectively represents the dynamics of $\langle \bar{z}_{T1} \rangle_{AC}$ by itself. Now, using the identities $\sin(2\omega_0 t) = 2\sin(\omega_0 t)\cos(\omega_0 t)$ and $2\sin^2(\omega_0 t) = 1 - \cos(2\omega_0 t)$ in (69) yields the following expression:

$$\left\langle \dot{\bar{z}}_{T1} \right\rangle_{AC} = \frac{P_0}{3C}\cos(2\omega_0 t) - \frac{LP_0^2\omega_0}{6Cv_{S,RMS}^2}\sin(2\omega_0 t). \tag{70}$$

Finally, $\langle \bar{z}_{T1} \rangle_{AC}$ is obtained by integrating both sides of (70) with respect to time, which yields

$$\langle \bar{z}_{T1} \rangle_{AC} = \frac{P_0}{6\omega_0 C}\sin(2\omega_0 t) + \frac{LP_0^2}{12Cv_{S,RMS}^2}\cos(2\omega_0 t). \tag{71}$$

As above mentioned, the constant term associated to the integration of (71) implies a DC offset, which is not a part of the AC solution, and thus it can be omitted. Consider that, indeed, initial values to solve $\langle \dot{\bar{z}}_{T1} \rangle_{AC}$ imply some departing condition at, typically, $t=0$, which, in this case, are rather the steady-state conditions previously solved and substituted. Thus, the full expression for $\bar{z}_{T1}$ in the steady state is given by

$$\bar{z}_{T1} = \langle \bar{z}_{T1} \rangle_{DC} + \langle \bar{z}_{T1} \rangle_{AC} \tag{72}$$

$$= \frac{E^2}{n} + \frac{P_0}{6\omega_0 C}\sin(2\omega_0 t) + \frac{LP_0^2}{12Cv_{S,RMS}^2}\cos(2\omega_0 t),$$

where the second harmonic component clearly comes out.

Regarding the harmonic content of z_{D1}, expression (23) can be solved with the same rational and following a similar procedure. The direct substitution of (62)-(64) and (68) into (23) produces

$$2C\left\langle \dot{\bar{z}}_{D1} \right\rangle_{AC} = \left[\frac{P_0 E}{v_{S,RMS}^2} - \frac{4P_0}{3E} \right] v_{S1} - \frac{2LP_0^2\omega_0\varphi_1}{3Ev_{S,RMS}^2}, \tag{73}$$
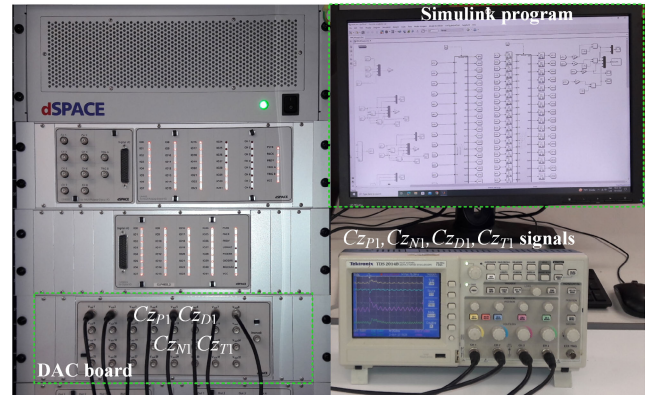
$$\left\langle \dot{\bar{z}}_{D1} \right\rangle_{AC} = \sqrt{\frac{2}{3}}\left[\frac{P_0 E}{2Cv_{S,RMS}} - \frac{2P_0 v_{S,RMS}}{3EC} \right]\sin(\omega_0 t)$$
$$- \frac{\sqrt{2}LP_0^2\omega_0}{3\sqrt{3}ECv_{S,RMS}}\cos(\omega_0 t), \tag{74}$$

where (65) and (67) have also been used.

Integrating both sides of (74) with respect to time yields the AC component of $\bar{z}_{D1}$, i.e.,

$$\langle \bar{z}_{D1} \rangle_{AC} = -\frac{\sqrt{2}}{\sqrt{3}\omega_0}\left[\frac{P_0 E}{2Cv_{S,RMS}} - \frac{2P_0 v_{S,RMS}}{3EC} \right]\cos(\omega_0 t)$$
$$- \frac{\sqrt{2}LP_0^2}{3\sqrt{3}ECv_{S,RMS}}\sin(\omega_0 t). \tag{75}$$

Again, integration with respect to time of the RHS of (75) would have yielded a DC offset that can be omitted. Furthermore, $\langle \bar{z}_{D1} \rangle_{DC} = 0$, making $\bar{z}_{D1} = \langle \bar{z}_{D1} \rangle_{AC}$, clearly exhibiting the fundamental frequency component.

IV. RTS EVALUATION

The MMC model (1)-(3), as well as the control and modulation schemes shown in Figure 3 were implemented in an RTS platform based on the DS1007 board from dSPACE. All equations describing the MMC and the controllers were discretized. The discretization method used for the plant was the Euler's forward rectangular approximation [28]; the resonant controllers and notch filters were discretized following the exact discretization method [29], and the discrete version of the PI controllers in the energy loops were obtained using the Euler's backward rectangular approximation [28]. Figure 4 shows the experimental setup used to carry out all tests.

The sampling frequency for the control scheme was set to 12 kHz, while the sampling frequency for the MMC was 108 kHz. This last value is 9 times the sampling frequency of the controller and is high enough to accurately represent the MMC model obtained via the Euler's approximation, as compared to the continuous-time system. It was observed that keeping the MMC model sampling frequency at an

integer multiple of the control sampling frequency resulted in cleaner signals.

The sampling frequency of the controller was selected based on the effective switching frequency of the MMC. Each cell is inserted or bypassed using a fixed switching frequency of 1 kHz. As there are six cells per phase, the effective switching frequency of the MMC is 6 kHz. Therefore, this is the minimum value that can be used for the sampling frequency of the controller, or an integer multiple of it. In this work, the sampling frequency of the controller was selected as twice the effective switching frequency of the MMC, i.e., 12 kHz.

The following parameter values were used for MMC: a DC-link voltage of E=630 V, three cells on each arm (n=3), a capacitance of C=4.7 mF (same on every cell), an inductance of L=7.5 mH (same on each arm), a pure sinusoidal and balanced three-phase grid voltage with a fundamental frequency of f_0=60 Hz and a line-to-line RMS voltage $v_{S,RMS}$=400 V_{RMS}, and a load power P_0 fluctuating between 15 kW and 21 kW.

The control parameters were tuned according to the conditions presented in Section III-E. Injected current loop: R_D=6 and σ_D=300. Circulating current loop: R_T=5 and σ_T=300. Energy regulation loop: k_{pT}=0.001 and k_{iT}=0.05. Energy balance loop: k_{pD}=0.5 and k_{iD}=0.001. The notch filters used to clean the signals as described in (47) and (48): γ_T=γ_D=40.

The frequency of the triangular carrier waveforms, for the PSC-PWM, was set to f_c=1 kHz. Each arm comprises three cells; hence, three triangular carriers were required per arm on each phase. The three triangular carriers guard a phase-shift from one another of $\boldsymbol{\phi}$= $[0, 2\pi/3, 4\pi/3]^\top$ rad. Moreover, the same set of three carriers was used for the upper and lower arms on all three phases, as recommended in [9] since the number of cells on each arm was odd.

The performed tests comprise (i) steady-state responses; (ii) transient responses under load step changes; and (iii) transient responses due to a reset of initial conditions of the capacitor voltages with unbalance. The latter was intended to show the natural balancing mechanism of capacitor voltages under the PSC-PWM scheme [23]. In addition to guaranteeing the natural tension balance of the cells, the PSC-PWM also allows the MMC to reach efficiencies of around 99.5% [30], [31]. All plots include a right arrow mark to the left of the corresponding curve indicating the corresponding DC offset, allowing the curves to be zoomed in and showing more detail.

A. STEADY-STATE RESPONSES

This test was performed considering a fixed load power of P_0=15 kW. The steady state responses of the three-phase MMC-based inverter, in closed loop with the overall proposed controller, are presented in Figures 5-8. Due to space limitations, most plots only show the responses for phase 1; in fact, the responses of the other two phases are quite similar. Figure 5 shows the steady-state responses of
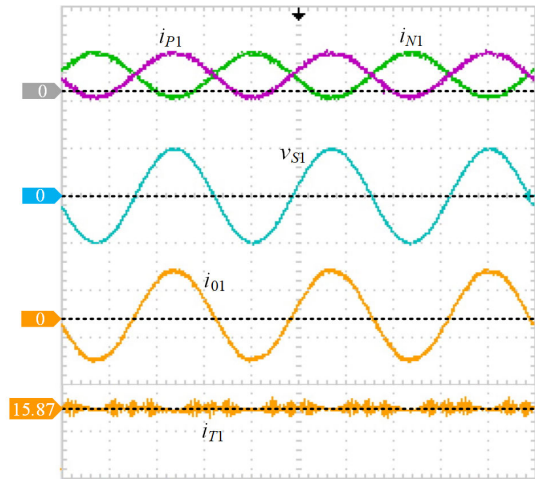

FIGURE 5. Steady-state responses (x-axis 5 ms/div) of (from top to bottom) the arm currents i_{P1} and i_{N1} (y-axis 31 A/div), the grid voltage v_{S1} (y-axis 325 V/div), the injected current i_{01} (y-axis 31 A/div), and the circulating current i_{T1} (y-axis: 13 A/div).

(top plot) the currents on the upper and lower arms i_{P1} and i_{N1}, respectively, which are biased oscillating signals as expected. In fact, the oscillation is mainly a sinusoidal at the fundamental frequency. Notice that (the two plots in the middle) the injected (differential-mode) current i_{01} reaches a sinusoidal shape with zero phase-shift (as required in this example) with respect to the corresponding grid voltage v_{S1}, thus, approaching a unitary power factor (PF).

Grid voltage sources were internally generated as pure balanced sinusoidal signals, while the injected currents, experimentally obtained, reached a THD of 1.1425%, a value well below the 5% required in the IEEE 519-2022 standard [32].

In its turn, (bottom plot) the circulating (common-mode) current i_{T1} resulted in an oscillating signal biased by a DC component. The slight ripple observed in the i_{T1} is due to the effect of the switching at the (common-mode) total inserted voltage e_{T1}, plus low frequency oscillations propagated through the reference $\mathbf{i}_T^*$. Recall that the construction of this later involves the feedback of the arms energies through the energy regulation and balance loops, where the arm energies are contaminated with low frequency oscillations.

According to [33], the way in which carriers were used in this work leads to output voltages with low harmonic distortion, while the circulating currents must exhibit odd harmonics of the switching frequency.

Figure 6 shows (top plots) the inserted voltages in the upper and lower arms, e_{P1} and e_{N1}, respectively; as well as (the two next plots) the control voltages e_{D1} and e_{T1}. Notice that e_{D1} is a staircase signal close to a sinusoidal, exhibiting the expected 7 levels (n=3, and thus $2n+1$=7), i.e., mainly comprising a fundamental component with very small amount of switching ripple at 6 kHz (6 times the carriers' frequency f_c). In fact, e_{D1} can be interpreted as the differential-mode voltage at the output of the MMC inverter feeding the load. The signal e_{T1} is a biased oscillating signal, with oscillations at
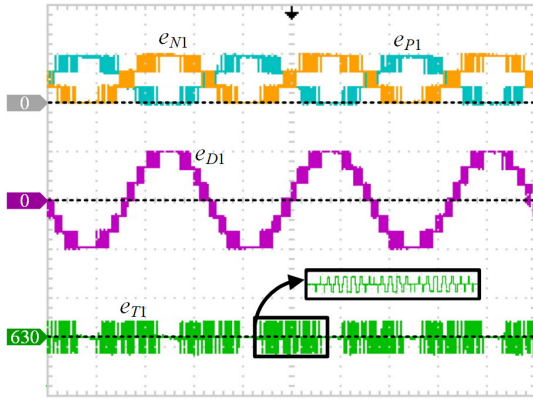
FIGURE 6. Steady-state responses (x-axis 5 ms/div) of (from top to bottom) the inserted voltages in the lower arm e_{N1} and the upper arm e_{P1} (y-axis: 630 V/div), the differential voltages by the lower and the upper arms e_{D1} (y-axis: 630 V/div), and the total voltage inserted by the lower and the upper arms e_{T1} (y-axis: 630 V/div).
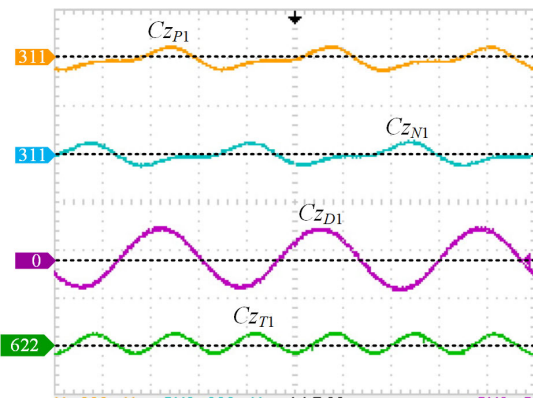

FIGURE 7. Steady-state responses (x-axis: 5 ms/div) of (from top to bottom) the total energies in the upper arm Cz_{P1} and the lower arm Cz_{N1} (y-axis: 35 J/div), the energy difference between the upper and the lower arm Cz_{D1} (y-axis: 20 J/div), and the total energy in the phase Cz_{T1} (y-axis: 28 J/div).

3 kHz, which can be interpreted as the common-mode voltage serving as the supply to produce the so-called circulating currents.

Figure 7 shows (from top to bottom) the accumulated energy of capacitor voltages at the upper arm Cz_{P1} and at the lower arm Cz_{N1}, the energy difference between the upper and the lower arms Cz_{D1}, and the total accumulated energy of both arms Cz_{T1} (state variables have been multiplied by C to recuperate the formal energy definition and the proper energy units). Notice that, besides the oscillation at the fundamental frequency, predicted in Section III-F, the energy difference Cz_{D1} reached zero (in average) after the accumulated energies of each arm (z_{P1} and z_{N1}) get balanced (in average). Meanwhile, Cz_{T1} included an oscillation at the second harmonic as predicted in Section III-F, which was mounted on a DC component of 622 J (i.e., $CE^2/3$) as expected.

Figure 8 shows the oscillating behavior of the upper arm capacitor voltages v_{C11}, v_{C21} and v_{C31}, and those of the lower arm v_{C41}, v_{C51} and v_{C61}. This figure shows that all
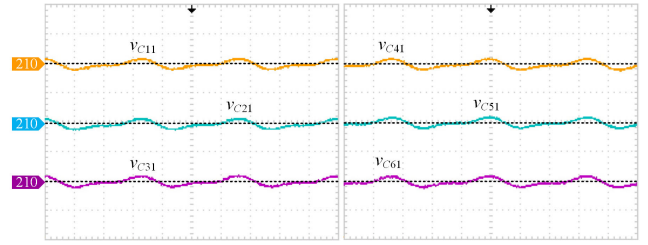

FIGURE 8. Steady-state responses (x-axis: 5 ms/div) of the capacitor voltages of (left plots) the upper arm v_{C11}, v_{C21} and v_{C31}; and (right plots) the lower arm v_{C41}, v_{C51} and v_{C61} (y-axis: 15 V/div).

capacitors are regulated (in average) to the same constant voltage reference of 210 V (i.e., E/n) as expected.

B. LOAD STEP CHANGES
In this test, the load power was changed step-wise going from P_0=15 kW to P_0=21 kW and back. Figure 9 shows the transient response due to this change on the load power conditions of (from top to bottom) the upper and lower arm currents i_{P1} and i_{N1}, respectively, as well as the circulating current i_{T1} and the injected current i_{01}. The latter is shown on top of v_{S1} to corroborate the in-phase requirement for a PF close to one. Notice that, besides the expected change on the amplitude of i_{01} in correspondence to the change of power, this current maintained an almost sinusoidal waveform in phase with the grid voltage after almost imperceptible transients. Currents i_{P1}, i_{N1} also maintained their biased sinusoidal waveform, which grows for a bigger load power demand. The amplitude of the circulating current i_{T1}, also referred to as the common-mode current, also followed the changes on the load power. Both variables reached the steady-state condition at approximately 75 ms.

Figure 10 shows the transient response of the control signals from the energy regulation loop Υ_{T1} and the energy balance loop P_{D1} (outcomes of the PI controllers). Notice that Υ_{T1} grew for a bigger power demand and stabilized after a relatively short transient around a constant value, which is reasonable as Υ_{T1} is the control signal that guarantees regulation of the total energy Cz_{T1} in the phase. As observed, this transient took about 50 ms. Besides, control signal P_{D1}, used to guarantee the balance between upper and lower energies, returned to zero (in average) after a transient of about 150 ms, i.e., three times longer than the transient of Υ_{T1}. Recall that Υ_{T1} and P_{D1} are used to build the reference for the circulating current i_{T1}^* according to (26), where it was observed that the effect of P_{D1} in i_{T1}^*, and thus in i_{T1}, was reduced due to scaling factors. In fact, P_{D1} had a considerable overshoot at the very beginning, but it vanished once the steady-state was reached. Hence, the shape of the transient observed in i_{T1} was mainly dominated by Υ_{T1}.

C. PHASE JUMP IN THE THREE-PHASE GRID VOLTAGE
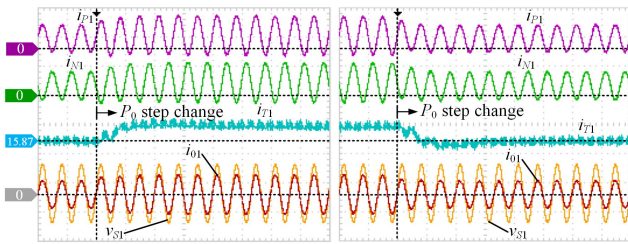In this test, a phase jump was introduced in the three grid voltages and in both directions $+30°$ (for leading) and

FIGURE 9. Transient responses (*x*-axis: 25 ms/div) of (from top to bottom) the arm currents i_{P1} and i_{N1} (*y*-axis: 31 A/div), the circulating current i_{T1} (*y*-axis: 13 A/div), and the injected current i_{01} (*y*-axis: 62 A/div), during a step change in the load power going from (left) P_0=15 kW to P_0=21 kW and (right) back from P_0=21 kW to P_0=15 kW. Grid voltage v_{S1} (*y*-axis: 325 V/div) is also included to show the zero phase-shift with i_{01}.
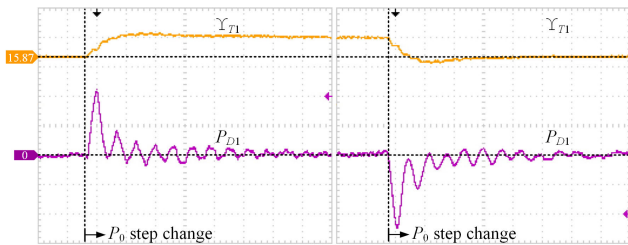

FIGURE 10. Transient responses (*x*-axis: 25 ms/div) of (from top to bottom) the control signals from the energy regulation loop Υ_{T1} (*y*-axis: 10 A/div) and the energy balance loop P_{D1} (*y*-axis: 640 W/div), during a step change in the load power going from (left) P_0=15 kW to P_0=21 kW and (right) from P_0=21 kW to P_0=15 kW.
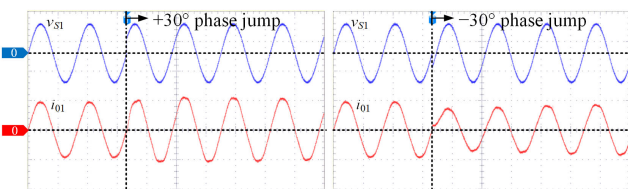

FIGURE 11. Transient responses (*x*-axis: 10 ms/div) of (from top to bottom) the grid voltage v_{S1} (*y*-axis 325 V/div) and the injected current i_{01} (*y*-axis 31 A/div), after (left) a jump of +30° and (right) a jump of −30° in the phase angle of the three-phase grid voltage.

−30° (for lagging), while maintaining a constant load power P_0=15 kW. The results for this experiment are shown in Figure 11. Notice that, after introducing a phase jump of +30°, the injected current slightly increased its amplitude during the transient. In contrast, after a phase jump of −30° was introduced, the current decreased its amplitude during the transient. After the transient, that only took few cycles, the current recovered its amplitude and kept synchronized with the grid voltage despite the phase jumps.

D. CAPACITOR VOLTAGES WITH UNBALANCED INITIAL CONDITIONS

For this test, the system was considered to be already in its steady state condition, then suddenly the voltages of the capacitors of each arm were reset to different values causing an instantaneous condition of imbalance between the voltages of the capacitors. It was preferred to realize
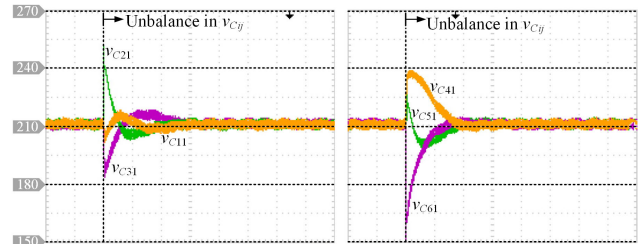

FIGURE 12. Transient responses (*x*-axis: 2.5 s/div) of the capacitor voltages in (left) the upper arm v_{C11}, v_{C21} and v_{C31}, and in (right) the lower arm v_{C41}, v_{C51} and v_{C61} (*y*-axis: 15 V/div), after the capacitors' voltages are suddenly reset to v_{C11}=210 V, v_{C21}=250 V, v_{C31}=190 V, v_{C41}=220 V, v_{C51}=210 V and v_{C61}=140 V.

this test starting from the steady state condition rather than from the start-up, just to observe, during the transient, the effect of a sudden unbalance in the capacitors voltages. Therefore, in this test, the capacitor voltages in the upper arms (of all phases), that were already in the steady state reaching 210 V, were suddenly reset to $v_{C1j}(0)$=210 V, $v_{C2j}(0)$=250 V and $v_{C3j}(0)$=190 V. For the lower arms, the capacitor voltages (in all phases), that were already in the steady state reaching also 210 V, were suddenly reset to $v_{C4j}(0)$=220 V, $v_{C5j}(0)$=210 V, and $v_{C6j}(0)$=140 V.

Figure 12 shows the transient responses of each capacitor voltage on phase 1 after suddenly resetting their values, and under the proposed control. Notice that, after a transient taking approximately 10 s, all v_{Cij} approached the 210 V (E/n) reference, which corroborates the natural balancing mechanism associated to the PSC-PWM scheme. However, this transient took considerably more time as compared to the transients of the rest of state variables in the system. Therefore, it is recommended adding an explicit algorithm to guarantee a faster balancing of the individual capacitors voltages.

Figure 13 shows the transient responses of the lower and upper arms total inserted voltages e_{N1} and e_{P1}, respectively; during (a) load power step change going from P_0=15 kW to P_0=21 kW; and (b) after the capacitors voltages are suddenly reset to v_{C11}=210 V, v_{C21}=250 V, v_{C31}=190 V, v_{C41}=220 V, v_{C51}=210 V and v_{C61}=140 V.

E. COMPARISON AGAINST PREVIOUSLY REPORTED CONTROL SCHEMES

The responses of the proposed controller are compared against those of control schemes reported in [25] and [34], with slight modifications to guarantee the fairest comparison possible. The tests consider the transient responses under load step changes and under unbalance in the capacitor voltages.

The control scheme in [25] considered a PI to regulate the output currents in the *dq*-coordinates, a PI and resonant (PIR) control for the circulating currents, a PI to regulate the overall energy in the three phases of the converter, a PI regulator for the energy on each phase, and a sorting algorithm for the capacitor voltages balancing. The controller [25] was modified to make a fair comparison. For this, the sorting
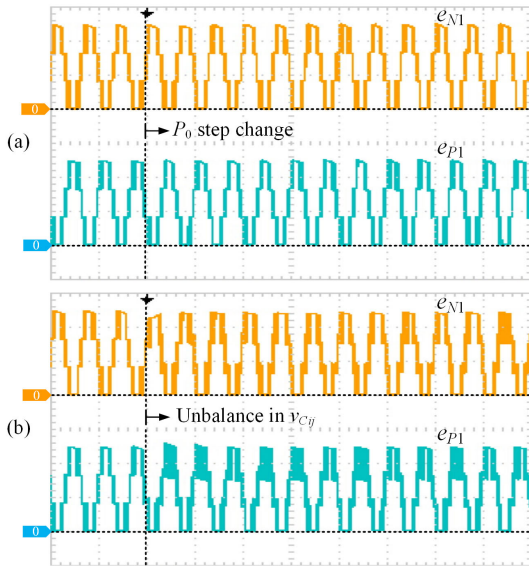
FIGURE 13. Transient responses of the lower and upper arms total inserted voltages e_{N1} and e_{P1} (y-axis: 252 V/div), (a) during a step change in the load power going from P_0=15 kW to P_0=21 kW; and (b) after the capacitors voltages are suddenly reset to v_{C11}=210 V, v_{C21}=250 V, v_{C31}=190 V, v_{C41}=220 V, v_{C51}=210 V and v_{C61}=140 V (in all plots x-axis: 25 ms/div).

FIGURE 14. Transient responses (in all plots x-axis: 20 ms/div) of (from top to bottom on each plot) the injected current i_{01} (y-axis: 31 A/div), and the circulating current i_{T1} (y-axis: 13 A/div); after a step change in the load power going from (plots to the left) P_0=15 kW to P_0=21 kW, and (plots to the right) back from P_0=21 kW to P_0=15 kW; under (a) the proposed controller, (b) the controller reported in [25], and (c) the controller in [34].

algorithm was replaced by a PI regulator for the energy balance between the upper and lower arms; moreover, the PI that regulates the overall energy in all phases has been omitted as well, as this regulator was concerned with the control of reactive current, that was not considered in our proposal. The control parameters considered in the modified [25] scheme are detailed next. Injected current loop: proportional gain 20 and integral gain 5; circulating current loop: proportional gain k_p=5, integral gain k_i=0.01, resonant gains ω_c=0.002π and k_r=150/ω_0; energy regulation loop: k_{pT}=0.001 and k_{iT}=0.05; energy balance loop: k_{pD}=0.5 and k_{iD}=0.001.

The control scheme in [34] considered a PI to regulate the average value of the capacitor voltages on each phase (averaging loop), a proportional controller weighted by an appropriate sign (depending on the sign of the arm currents) for each capacitor voltage (balancing loop), and a PI controller for the circulating currents. In this scheme no explicit control rules were given for the output currents, so the same control as in the proposed controller is considered for these variables. The control parameters considered for the scheme [34] are detailed next. Injected current loop: R_D=6 and σ_D=300; circulating current loop: proportional gain K_3=5 and integral gain K_4=0.7958; averaging loop: proportional gain K_1=0.5 and integral gain K_2=1; balancing loop: proportional gain K_5=2.5.

1) LOAD STEP CHANGES

Figure 14 shows the transient responses of (a) the proposed controller, (b) the controller reported in [25], and (c) the controller reported in [34], after the load power is changed from **(left plots)** P_0=15 kW to P_0=21 kW and
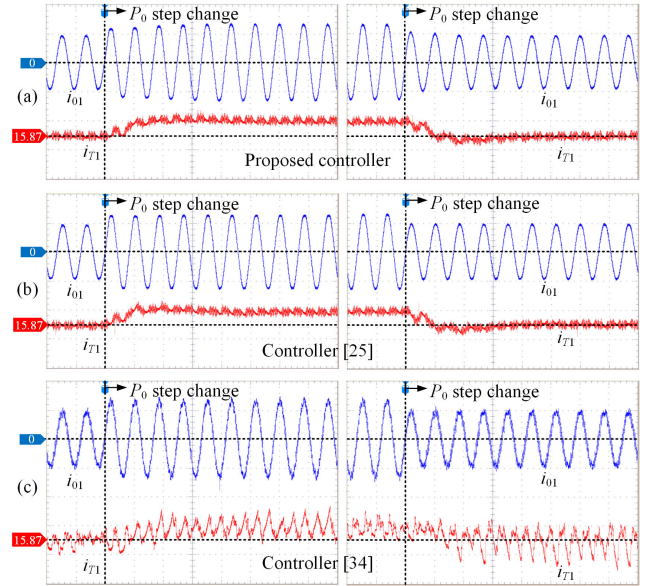
(right plots) from P_0=21 kW to P_0=15 kW. Each graph of all three controllers shows (top signal) the injected current and (bottom signal) the circulating current. The tests revealed that the proposed scheme and the [25] modified scheme yielded very similar results. However, the currents obtained with [34] scheme exhibited more deteriorated waveforms, that is, a perceptible ripple is observed in the injected current as well as in the circulating current when compared to the responses with the proposed control.

2) CAPACITOR VOLTAGES WITH UNBALANCED INITIAL CONDITIONS

For the sake of comparison, the controllers reported in [25] and [34] were also exposed to the same test described in Subsection IV-D, that is, the capacitor voltages in the upper arms (of all phases) were suddenly reset from their steady state value of 210 V to $v_{C1j}(0)$=210 V, $v_{C2j}(0)$=250 V and $v_{C3j}(0)$=190 V; while, for the lower arms, the capacitor voltages (in all phases) were suddenly reset from their steady state value of 210 V to $v_{C4j}(0)$=220 V, $v_{C5j}(0)$=210 V, and $v_{C6j}(0)$=140 V. As a consequence, the upper and lower arms stored energy $Cz_{Pj}(0)$ and $Cz_{Nj}(0)$ also suddenly changed their values from 311 J in the steady state to Cz_{P1}=335.35 J (8% above) and Cz_{Nj}=263.44 J (15% below), respectively; and thus their difference and their sum took the sudden values Cz_{D1}=71.91 J and Cz_{T1}= 598.79 J. Figure 15 shows the transient response due to the aforementioned reset on the capacitor voltage conditions under **(a)** the proposed controller, **(b)** the controller reported in [25], and **(c)** the controller reported in [34].
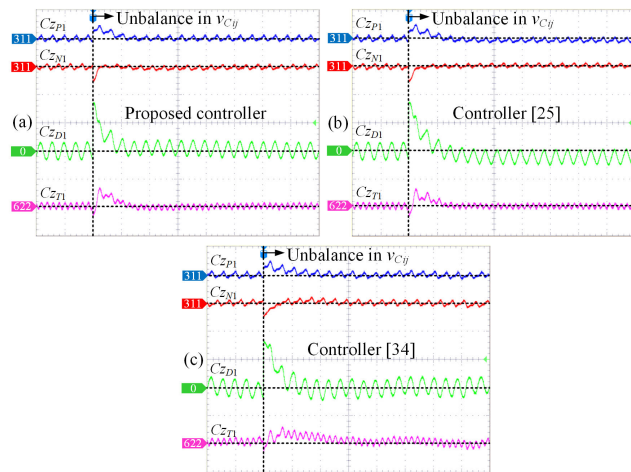
FIGURE 15. Transient responses (in all plots x-axis: 40 ms/div) of (from to top to bottom on each plot) the total energies in the upper arm Cz_{P1} and the lower arm Cz_{N1} (y-axis: 88 J/div), the energy difference between the upper and the lower arm Cz_{D1} (y-axis: 40 J/div), and the total energy in the phase Cz_{T1} (y-axis: 62 J/div), under (a) the proposed controller, (b) the controller reported in [25], and (c) the controller reported in [34].

TABLE 1. Performance parameters comparison.

Parameter	Proposed controller	Controller [25]	Controller [34]
$t_s \ Cz_{N1}$	40 ms	40 ms	120 ms
i_{T1} RMS error	1.12 A	1.49 A	5.15 A
i_{01} THD	1.1%	1.1%	3.0%
Execution time	0.90 μs	0.98 μs	1.04 μs

Notice that, under the proposed controller, Cz_{D1} and Cz_{T1} reached their references in approximately 120 ms and 50 ms, respectively, a considerable shorter time than that observed in the individual capacitor voltages' responses. As a matter of fact, recall that control actions are only exerted on the energies, leaving the balance of the individual capacitor voltages to the modulation scheme, which explains why the energy variables reached the steady-state condition faster than the capacitor voltages. The controller of [25] allowed Cz_{T1} to reach its reference also in 50 ms approximately; however, the energy difference Cz_{D1} was maintained at steady state slightly below its reference value. Finally, it was observed that, in the controller [34], both Cz_{D1} and Cz_{T1} maintained oscillations at low non-characteristic frequencies around their reference values.

Table 1 shows a comparison between some performance parameters obtained with the proposed controller and the controllers reported in [25] and [34]. The parameters included in this comparison are those in which a noticeable difference appears, as other performance parameters achieve similar results. It is observed that the proposed controller and the controller [25] achieve similar injected current i_{01} THD, as well as similar settling time t_s in the response of lower arm energy Cz_{N1}. Notice that the proposed controller showed the smallest execution time of the algorithm (realized in the dSPACE board). It is also observed that the proposed scheme gets the smallest circulating current i_{T1} RMS error, which is

calculated as the RMS value of the difference between i_{T1} and its steady state value of 15.87 A (at the lower power demand $P_0 = 15$ kW). In contrast, the controller [34] showed the worst performance among the three algorithms in the parameters considered in Table 1.

V. CONCLUSION

This work presented an energy model-based controller for a three-phase modular multilevel converter (MMC) topology of $2n+1$ levels used in a grid tied application. A mathematical model of the three-phase MMC was developed in this work, that consisted in the sum and difference of the arm currents and arm energies. These represented suitable state-variables that facilitated the control design process as they lead to a decoupled model representation, which in its turn allows to split the control design into four loops. Overall, the proposed control scheme guaranteed tracking of the output and circulating currents towards their references, as well as energy regulation and energy balance of the MMC arms. In addition to the MMC modelling and control design, tuning rules of every involved parameter in the control scheme were provided. Moreover, to achieve voltage balance at the cell level, the designed controller was augmented with the phase-shifted carrier-based pulse-width modulation (PSC-PWM), a well known modulation scheme to provide a natural balancing mechanism for the individual capacitor voltages. The performance of the MMC-based inverter in closed-loop with the proposed control, including the PSC-PWM scheme, was evaluated in a real-time simulation platform using the DS1007 processor board from dSPACE. The case study considered an MMC of 7 levels ($n=3$), and the tests included load step changes and a sudden reset of capacitor voltages values to create an unbalanced condition (in all phases) to observe the transient behaviors of the variables of interest. These results showed that the proposed controller guaranteed a relatively fast response maintaining the energy variables in their references (in average). It was also observed that the PSC-PWM scheme was able to ensure balance of the individual capacitors voltages as claimed in the literature, albeit at a slower rate. Future work must include the design of a controller to guarantee a good performance of the MMC even under perturbations in the grid voltage such as unbalance or/and harmonic distortion.

REFERENCES

[1] M. Priya, P. Ponnambalam, and K. Muralikumar, "Modular-multilevel converter topologies and applications—A review," *IET Power Electron.*, vol. 12, no. 2, pp. 170–183, 2019.

[2] S. Prakash and M. B. N. Mohamed, "Modular multilevel converter for renewable system towards THD mitigation," in *Proc. Int. Conf. Circuit Power Comput. Technol. (ICCPCT)*, Aug. 2023, pp. 830–834.

[3] A. Elsanabary, S. Mekhilef, M. Seyedmahmoudian, and A. Stojcevski, "A novel circuit configuration for the integration of modular multilevel converter with large-scale grid-connected PV systems," in *Proc. IEEE 12th Energy Convers. Congr. Expo. Asia (ECCE-Asia)*, May 2021, pp. 232–237.

[4] X. Li, Z. Xu, and Z. Zhang, "Application of MMC with embedded energy storage for overvoltage suppression and fault ride-through improvement in series LCC-MMC hybrid HVDC system," *J. Mod. Power Syst. Clean Energy*, vol. 11, no. 3, pp. 1001–1013, May 2023.

[5] R. O. D. Sousa, A. F. Cupertino, L. M. F. Morais, H. A. Pereira, and R. Teodorescu, "Experimental validation and reliability analyses of minimum voltage control in modular multilevel converter-based STATCOM," *IEEE Trans. Ind. Electron.*, early access, pp. 1–10, Aug. 2023. [Online]. Available: https://ieeexplore.ieee.org/document/10236896

[6] N. R. Karaka, P. R. Nallamatti, and A. Shukla, "Extended linear modulation based full bridge modular multilevel converter for adjustable speed drives," in *Proc. 25th Eur. Conf. Power Electron. Appl. (EPE ECCE Europe)*, Sep. 2023, pp. 1–7.

[7] A. I. Elsanabary, G. Konstantinou, S. Mekhilef, C. D. Townsend, M. Seyedmahmoudian, and A. Stojcevski, "Medium voltage large-scale grid-connected photovoltaic systems using cascaded H-bridge and modular multilevel converters: A review," *IEEE Access*, vol. 8, pp. 223686–223699, 2020.

[8] G. A. C. Contreras, G. Escobar, A. A. Valdez-Fernandez, and M. J. Lopez-Sanchez, "A current controller for the modular multilevel converter operating under distorted grid voltage," *Int. Trans. Electr. Energy Syst.*, vol. 28, no. 4, p. e2524, Apr. 2018.

[9] G. A. Catzin Contreras, G. Escobar, A. A. Valdez-Fernandez, and M. J. Lopez-Sanchez, "A model-based controller for a single-phase grid-tied modular multilevel inverter with regulation and balance of energy," *Int. Trans. Electr. Energy Syst.*, vol. 29, no. 8, pp. 1–17, Aug. 2019.

[10] H. Xu, M. Gao, P. Ge, and J. Hu, "Linear active disturbance rejection control and stability analysis for modular multilevel converters under weak grid," *J. Modern Power Syst. Clean Energy*, vol. 11, no. 6, pp. 2028–2042, Nov. 2023.

[11] P. K. Kar, A. Priyadarshi, and S. B. Karanki, "Development of an enhanced multilevel converter using an efficient fundamental switching technique," *Int. J. Electr. Power Energy Syst.*, vol. 119, Jul. 2020, Art. no. 105960.

[12] O. C. Sakinci and J. Beerten, "Equivalent multiple *dq*-frame model of the MMC using dynamic phasor theory in the $\alpha\beta z$-frame," *IEEE Trans. Power Del.*, vol. 35, no. 6, pp. 2916–2927, Dec. 2020.

[13] Y. Xu, Z. Xu, Z. Zhang, and H. Xiao, "A novel circulating current controller for MMC capacitor voltage fluctuation suppression," *IEEE Access*, vol. 7, pp. 120141–120151, 2019.

[14] Z. Yang, P. Song, J. Song, X. Wang, and X. Li, "An MMC circulating current suppressing controller based on bridge arm common-mode voltage," *IEEE Access*, vol. 8, pp. 189471–189478, 2020.

[15] M. Utvić and D. Dujić, "Generalized theory on direct arm energy control in modular multilevel converters," *CPSS Trans. Power Electron. Appl.*, vol. 5, no. 4, pp. 388–399, Dec. 2020.

[16] G. A. Catzin-Contreras, A. A. Valdez-Fernandez, G. Escobar, and M. J. Lopez-Sanchez, "A model-based controller for a three-phase grid-connected modular multilevel converter," in *Proc. IEEE Int. Autumn Meeting Power, Electron. Comput. (ROPEC)*, Ixtapa, Mexico, Nov. 2015, pp. 1–6.

[17] D. Dinkel, C. Hillermeier, and R. Marquardt, "Direct multivariable control for modular multilevel converters," *IEEE Trans. Power Electron.*, vol. 37, no. 7, pp. 7819–7833, Jul. 2022.

[18] M. H. Nguyen and S. Kwak, "Predictive nearest-level control algorithm for modular multilevel converters with reduced harmonic distortion," *IEEE Access*, vol. 9, pp. 4769–4783, 2021.

[19] Z. Wang, X. Yin, and Y. Chen, "Model predictive arm current control for modular multilevel converter," *IEEE Access*, vol. 9, pp. 54700–54709, 2021.

[20] M. M. Raja, H. Wang, M. H. Arshad, G. J. Kish, and Q. Zhao, "Data driven model predictive control for modular multilevel converters with reduced computational complexity," *IEEE Access*, vol. 11, pp. 42113–42123, 2023.

[21] H. M. Ismail and S. Kaliyaperumal, "Enhanced voltage sorting algorithm for balancing the capacitor voltage in modular multilevel converter," *IEEE Access*, vol. 9, pp. 167489–167502, 2021.

[22] X. Gao, W. Tian, Q. Yang, N. Chai, J. Rodriguez, R. Kennel, and M. L. Heldwein, "Model predictive control of a modular multilevel converter considering control input constraints," *IEEE Trans. Power Electron.*, vol. 39, no. 1, pp. 636–648, Jan. 2024.

[23] W. van der Merwe, P. Hokayem, and L. Stepanova, "Analysis of the 5-cell single phase MMC natural balancing mechanism," in *Proc. IEEE Energy Convers. Congr. Expo. (ECCE)*, Pittsburgh, PA, USA, Sep. 2014, pp. 3416–3423.

[24] L. Harnefors, A. Antonopoulos, S. Norrga, L. Angquist, and H.-P. Nee, "Dynamic analysis of modular multilevel converters," *IEEE Trans. Ind. Electron.*, vol. 60, no. 7, pp. 2526–2537, Jul. 2013.

[25] Z. Wang, A. Zhang, H. Zhang, and Z. Ren, "Control strategy for modular multilevel converters with redundant sub-modules using energy reallocation," *IEEE Trans. Power Del.*, vol. 32, no. 3, pp. 1556–1564, Jun. 2017.

[26] A. A. Valdez-Fernández, P. R. Martínez-Rodríguez, G. Escobar, C. A. Limones-Pozos, and J. M. Sosa, "A model-based controller for the cascade H-bridge multilevel converter used as a shunt active filter," *IEEE Trans. Ind. Electron.*, vol. 60, no. 11, pp. 5019–5028, Nov. 2013.

[27] G. Escobar, P. R. Martinez-Rodriguez, C. N. M. Ho, and J. M. Sosa, "Design of an inverter-side current reference and controller for a single-phase LCL-based grid-connected inverter," *Int. Trans. Electr. Energy Syst.*, vol. 28, no. 1, p. e2476, Jan. 2018.

[28] G. F. Franklin, J. D. Powell, and M. L. Workman, *Digital Control of Dynamic Systems*, 3rd ed. Menlo Park, CA, USA: Addison-Wesley, 1997, ch. 3, pp. 59–60.

[29] K. Ogata, *Discrete-Time Control Systems*, 2nd ed. Upper Saddle River, NJ, USA: Prentice-Hall, 1995, ch. 5, pp. 314–358.

[30] A. Hassanpoor, S. Norrga, and A. Nami, "Loss evaluation for modular multilevel converters with different switching strategies," in *Proc. 9th Int. Conf. Power Electron. ECCE Asia (ICPE-ECCE Asia)*, Jun. 2015, pp. 1558–1563.

[31] A. O. Arslan, F. Eroğlu, M. Kurtoğlu, and A. M. Vural, "Effect of arm inductance on efficiency of modular multilevel converter," in *Proc. 2nd Int. Symp. Multidisciplinary Stud. Innov. Technol. (ISMSIT)*, Ankara, Turkey, Oct. 2018, pp. 1–4.

[32] *IEEE Standard for Harmonic Control in Electric Power Systems*, IEEE Standard 519-2022, Revision IEEE Standard 519-2014, 2022, pp. 1–31.

[33] B. Li, R. Yang, D. Xu, G. Wang, W. Wang, and D. Xu, "Analysis of the phase-shifted carrier modulation for modular multilevel converters," *IEEE Trans. Power Electron.*, vol. 30, no. 1, pp. 297–310, Jan. 2015.

[34] M. Hagiwara and H. Akagi, "Control and experiment of pulsewidth-modulated modular multilevel converters," *IEEE Trans. Power Electron.*, vol. 24, no. 7, pp. 1737–1746, Jul. 2009.

GLENDY ANYALI CATZIN-CONTRERAS (Member, IEEE) received the M.Eng. degree in renewable energies from the School of Engineering, Autonomous University of Yucatan (UADY), Mexico, in 2014, and the Ph.D. degree in electronics engineering from the School of Sciences, Autonomous University of San Luis Potosi (UASLP), Mexico, in 2018. She is currently a Postdoctoral Researcher with the School of Engineering and Sciences, Tecnologico de Monterrey, Nuevo Leon, Mexico. Her research interests include the modeling of switched converters, the repetitive control for harmonic compensation, signal processing, and real-time simulations. She is a candidate member of the National Research Fellows System (SNI-C), CONAHCyT, Mexico.

GERARDO ESCOBAR (Senior Member, IEEE) received the Ph.D. degree in automatic control from the Signals and Systems Laboratory LSS-SUPELEC, Université de Paris XI, France, in 1999. From 2008 to 2012, he was a Principal Scientist with the Power Electronics Group, ABB Switzerland Ltd., Zürich, Switzerland. He is currently a Professor/Researcher and the Leader of the Research Group on Energy Conversion, Storage and Management, School of Engineering and Sciences, Tecnologico de Monterrey, Nuevo Leon, Mexico. His main research interests include modeling, analysis, and the control design of power electronic systems, and their applications. He is a member of the National Research Fellows System level 3 (SNI-3), CONAHCYT, Mexico. He was an Associate Editor (AE) of IEEE TRANSACTIONS ON INDUSTRIAL ELECTRONICS, from 2007 to 2016. He has been an AE of IEEE TRANSACTIONS ON POWER ELECTRONICS, since 2013.

JESUS ELIAS VALDEZ-RESENDIZ (Senior Member, IEEE) received the M.Eng. degree in electrical engineering from Instituto Tecnologico de Ciudad Madero, Madero, Mexico, in 2011, and the Ph.D. degree in electronics engineering from the Centro Nacional de Investigación y Desarrollo Tecnologico, Cuernavaca, Mexico, in 2016. From 2016 to 2017, he was a Postdoctoral Fellow with Tecnologico de Monterrey, Monterrey, Mexico, where he is currently an Assistant Professor in electrical engineering. He is a member of the National Research Fellows System level 1 (SNI-1), CONAHCYT, Mexico. He is also an Associate Editor of the *Mathematical Problems in Engineering* and the *International Transactions on Electrical Energy Systems* journals and the Chair of the professional chapter of IEEE Power Electronics Society (PELS) in the Monterrey Section. His research interests include power electronics, energy management, energy conversion, and electric vehicles.

ANDRES A. VALDEZ-FERNANDEZ (Senior Member, IEEE) received the Ph.D. degree in control and dynamical systems from the Potosi Institute of Scientific and Technological Research (IPICyT), Mexico, in 2009. From 2008 to 2012, he was a full-time Professor/Researcher with the National Technological Institute of Mexico, Technological Institute of Sperior Studies of Irapuato (TecNM-ITESI), Mexico. He is currently a full-time Professor/Researcher with the School of Sciences, Universidad Autonoma de San Luis Potosi (UASLP), Mexico. His research interests include analysis, modeling, control design, and the fault diagnosis of active power filters, inverters, rectifiers, renewable energy systems, and e-mobility systems. He is a member of the National Research Fellows System level 2 (SNI-2), CONAHCYT, Mexico.

● ● ●

LUIS IBARRA (Senior Member, IEEE) received the B.Eng. degree in mechatronics and the Ph.D. degree in intelligent control from Tecnologico de Monterrey, Mexico City, in 2011 and 2016, respectively. He has participated in numerous consulting activities associated with monitoring and control equipment for power systems and electric machinery, automation systems, and in the planning of distributed energy resources deployment. He is currently a Researcher with the Institute of Advanced Materials for Sustainable Manufacturing, Tecnologico de Monterrey. In addition, he is a founding partner of a technology company. His main research interests include power systems, automatic control, electric machinery, signal processing, and applied artificial intelligence. He is a member of the National Research Fellows System level 1 (SNI-1), CONAHCYT, Mexico.